ACS APPLIED MATERIALS & INTERFACES

www.acsami.org

Research Article

Bottom-Up Synthesis of SnTe-Based Thermoelectric Composites

Bingfei Nan, Xuan Song, Cheng Chang, Ke Xiao, Yu Zhang, Linlin Yang, Sharona Horta, Junshan Li, Khak Ho Lim, Maria Ibáñez,* and Andreu Cabot*

Cite This: *ACS Appl. Mater. Interfaces* 2023, 15, 23380−23389

Read Online

ACCESS | Metrics & More | Article Recommendations | Supporting Information

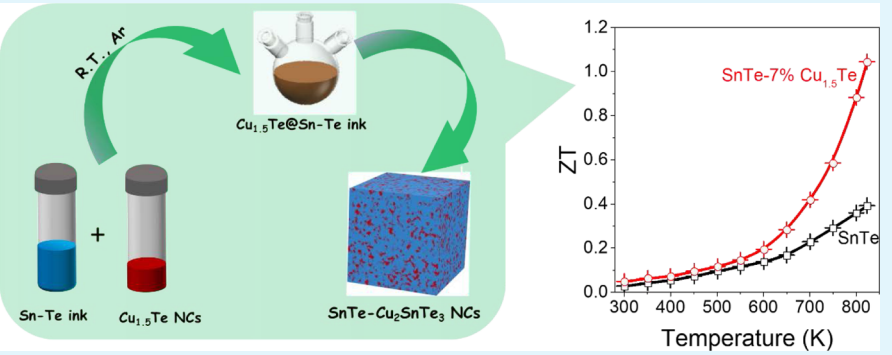

ABSTRACT: There is a need for the development of lead-free thermoelectric materials for medium-/high-temperature applications. Here, we report a thiol-free tin telluride (SnTe) precursor that can be thermally decomposed to produce SnTe crystals with sizes ranging from tens to several hundreds of nanometers. We further engineer SnTe−Cu_2SnTe_3 nanocomposites with a homogeneous phase distribution by decomposing the liquid SnTe precursor containing a dispersion of $Cu_{1.5}Te$ colloidal nanoparticles. The presence of Cu within the SnTe and the segregated semimetallic Cu_2SnTe_3 phase effectively improves the electrical conductivity of SnTe while simultaneously reducing the lattice thermal conductivity without compromising the Seebeck coefficient. Overall, power factors up to 3.63 mW m^{-1} K^{-2} and thermoelectric figures of merit up to 1.04 are obtained at 823 K, which represent a 167% enhancement compared with pristine SnTe.

KEYWORDS: *tin telluride, copper telluride, thermoelectric, Cu_2SnTe_3, molecular precursor, nanocomposite*

INTRODUCTION

Thermoelectric (TE) materials enable the direct and reversible conversion between thermal and electrical energies.[1] Owing to the omnipresence of thermal energy, the development of TE devices to power wireless sensors, recover waste heat, and regulate temperature is attracting increasing attention.[2,3] Toward harvesting energy, while thermal energy is ubiquitous, the energy conversion efficiency of the TE device determines its size and thus cost-effectiveness. Aside from thermal and electric contacts, this energy conversion efficiency can be estimated from a dimensionless figure of merit (ZT) of the TE material, defined as $ZT = \frac{S^2\sigma T}{\kappa_{tot}} = \frac{S^2\sigma T}{\kappa_L + \kappa_e}$, where S, σ, T, and κ_{tot} are, respectively, the Seebeck coefficient, electrical conductivity, absolute temperature, and total thermal conductivity that includes a lattice κ_L and an electronic κ_e component. Unfortunately, the interdependencies among these parameters make the optimization of TE materials an extremely difficult task.

TE parameters strongly depend on the temperature. While ambient temperature applications are dominated by devices based on Bi−Sb−Te−Se alloys,[4−7] in the medium-/high-temperature range (600−800 K), lead chalcogenides provide the highest ZT values.[8−11] However, the presence of toxic Pb in these materials is a major drawback toward commercialization.[12,13] Tin telluride (SnTe), a group IV−VI semiconductor with similar crystal and band structures to PbTe, is a particularly suitable alternative TE material for the medium-/high-temperature range.[14−16] Nevertheless, a too large carrier concentration (~10^{20} to 10^{21} cm^{-3}) originating from a high density of Sn vacancies, a too-narrow band gap (~0.18 eV at 300 K), and a high energy offset (~0.35 eV at 300 K) between the light valence band L and the heavy valence band Σ result in elevated thermal conductivities and moderate Seebeck coefficients and thus an overall poor TE performance.[17,18]

Several strategies have been developed to improve the TE properties of SnTe, including energy filtering,[19,20] band

Received: January 18, 2023
Accepted: April 21, 2023
Published: May 4, 2023

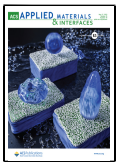

convergence,[21,22] hyperconvergence,[23,24] Rashba effect,[25] introduction of resonant levels,[12] modulation of defects,[26] incorporation of dense dislocations and precipitates,[27] and combinations of these approaches.[13,28−31] Within these strategies, the incorporation of dopants and alloying phases into the SnTe matrix to form point defects and/or precipitates that act as strong phonon scattering centers is particularly effective. These phases include In_2Te_3,[32] CdSe,[33] $Cu_{1.75}Se$,[34] Cu_2Te,[35] SnS,[36] $AgBiTe_2$,[37] MgAgSb,[38] and $CuSbSe_2$.[39] In particular, copper has been introduced in an ionic form within the SnTe matrix and as segregated Cu-based phases. Both interstitial Cu atoms and segregated $Cu_2Te/Cu_{1.75}Te$ phases have been shown to effectively scatter phonons, resulting in extremely low lattice thermal conductivities down to 0.5 W m^{-1} K^{-1}.[40−44]

Synthetic approaches developed for SnTe-based materials include the high-temperature melting method,[13,45,46] mechanical alloying,[47] melt spinning,[48] self-propagating high-temperature synthesis,[49,50] solvothermal method,[51−54] microwave method,[55,56] and aqueous solution method.[57] Among them, the bottom-up engineering of composites using solution-processed nanocrystals as building blocks is a particularly scalable, low-cost, and extremely versatile approach to optimize the performance in numerous applications.[58−63] Within this approach, the use of inorganic ligands or molecular precursors to adjust the nanocrystal surface composition and to produce nanocomposites with controlled phase distribution has emerged as an especially suitable strategy.[64−69] In this direction, we have recently reported the preparation of tin chalcogenides such as $SnSe_2$,[70] SnSe,[71] and SnS_2[72] using molecular precursor inks. Besides, we recently demonstrated that a CdSe ligand could act as a secondary phase during the nanocomposite consolidation to modify the electronic band structure of the SnTe matrix, reaching ZT values up to 1.3 at 850 K.[73] We also recently demonstrated the effectiveness of a soluble PbS molecular complex in a thiol-amine solvent to modify the SnTe nanocrystal surface and produce SnTe−PbS nanocomposites, reaching ca. 0.8 ZT value at 873 K.[74]

Brutchey et al. showed a Sn−Te precursor solution dissolved using ethylenediamine and a thiol at a 4:1 volume rate, yielding crystalline SnTe with Te impurity after solution deposition and heat treatment at 250 °C.[75] While thiols offer evident safety advantages over extensively used hydrazine, they should also be prevented owing to health and safety issues and the potential contamination of the final material with sulfur.

Herein, we demonstrate the preparation of a SnTe precursor using a thiol-free solvent based on oleylamine (OAm) and tri-*n*-octylphosphine (TOP). This precursor allows producing pure SnTe at moderate decomposition temperatures. In contrast to previously reported procedures to produce SnTe nanocrystals,[73,76,77] the use of a Sn−Te precursor ink offers advantages in terms of the processability of printed SnTe-based devices. Besides, the SnTe ink can be combined with $Cu_{1.5}Te$ nanoparticles to produce Sn−Cu−Te nanocomposites upon thermal decomposition. Dense $SnTe−Cu_2SnTe_3$ nanocomposites are then obtained by a hot-press sintering process. Interestingly, the produced Cu_2SnTe_3 remarkably improves the power factor by increasing the electrical conductivity without deteriorating the Seebeck coefficient. At the same time, the lattice thermal conductivity is strongly decreased. As a result, record ZT values for this system are demonstrated.

RESULTS AND DISCUSSION

A SnTe precursor was prepared by coordinating Sn^{2+} ions with OAm to form a Sn−OAm complex and combining it with TOP telluride (TOPTe) (see details in the Supporting Information, Figures 1a and S1).[78,79] Figure 1b displays the

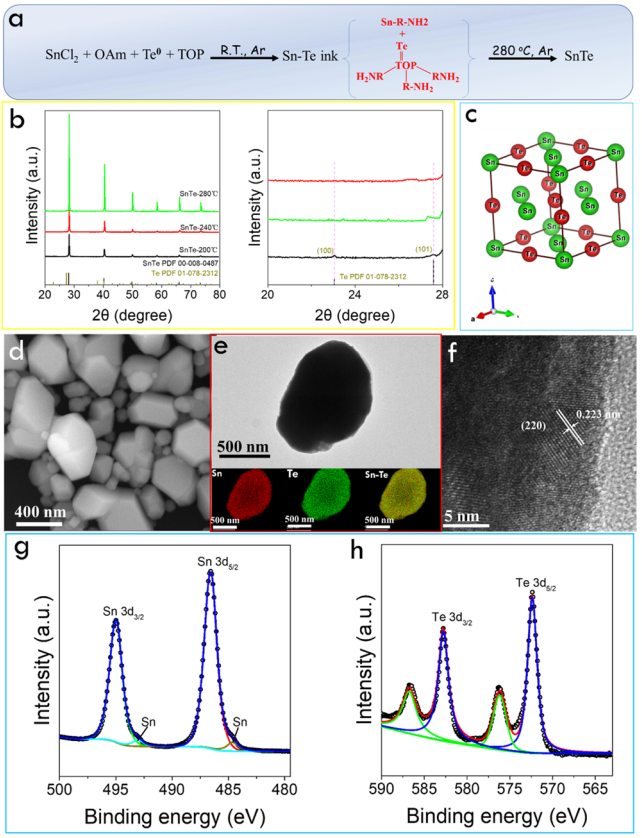

Figure 1. (a) Scheme of the formation of SnTe from the ink containing Sn−OAm and TOPTe complexes. (b) Powder XRD patterns of the material obtained from the SnTe precursor decomposed at different temperatures of 200, 240, and 280 °C. The graph on the right displays an expanded XRD pattern to show the presence of the Te phase. (c) Cubic rock-salt SnTe crystal phase. (d) SEM image of SnTe obtained at 280 °C. (e) TEM and EDX mapping of a SnTe particle. (f) HRTEM image of a SnTe particle. (g) and (h) High-resolution Sn 3d and Te 3d XPS spectra of SnTe obtained at 280 °C.

X-ray diffraction (XRD) pattern of the materials obtained from the decomposition of the Sn−Te ink at different temperatures. The XRD patterns display the diffraction peaks corresponding to the (200), (220), (222), (400), (420), and (422) planes of the cubic rock-salt SnTe crystal belonging to the *Fm*3*m* space group with a = 6.303 Å (Figure 1c). Additional peaks corresponding to Te impurities are found in the material obtained at 200 °C. Upon increasing the decomposition temperature from 200 to 280 °C, the impurity peaks disappear and the intensity of the cubic SnTe pattern increases, indicating a more effective reaction of Te and an improved SnTe crystallization and/or larger SnTe crystal domains.

Scanning electron microscopy (SEM) characterization showed a notable increase in the particle size with the reaction temperature (Figure S2). As shown in Figures 1d and S3, the SnTe particles obtained at 280 °C displayed a highly faceted morphology and a broad size distribution with an average size

https://doi.org/10.1021/acsami.3c00625
ACS Appl. Mater. Interfaces 2023, 15, 23380−23389

of 300 ± 200 nm. Energy-dispersive X-ray (EDX) analysis results revealed a slight excess of Sn, Sn/Te ∼1.1 (Table S1). This uncommon Sn-rich composition has been previously obtained using colloidal synthesis strategies, probably owing to the stabilization of Sn-terminated surfaces.[80] Previously synthesized pure SnTe particles usually exhibit octahedral-shaped structures with eight (111) planes because the surface energy of the (111) planes is lower than that of the (110) planes in Sn-poor SnTe particles.[81−83] Unlike the (111) dominance plane from Sn-poor SnTe particles, the preferential planes in Te-rich particles should be the (110) planes.[84,85] Transmission electron microscopy (TEM)-EDX maps showed a uniform distribution of Sn and Te at the nanometer scale (Figure 1e). Besides, high-resolution TEM (HRTEM) confirmed the cubic SnTe phase and the highly crystalline structure of the particles (Figure 1f).

Figure 1g,h displays the X-ray photoelectron spectroscopy (XPS) spectra of SnTe obtained at 280 °C. The high-resolution Sn 3d XPS spectrum exhibits one doublet at 495.1 eV (Sn $3d_{3/2}$) and 486.6 eV (Sn $3d_{5/2}$) associated with a Sn^{2+} oxidation state within a chalcogenide chemical environment.[45] A second small doublet appears at 493.1 and 484.7 eV, and it is ascribed to the presence of a small amount of metallic Sn.[86] The high-resolution Te 3d XPS spectrum exhibits two doublets. The main one is located at 582.8 eV (Te $3d_{3/2}$) and 572.4 eV (Te $3d_{5/2}$), and it is associated with Te^{2-} within a metal telluride chemical environment.[26] The second one is located at significantly higher binding energies, 586.7 (Te $3d_{3/2}$) and 576.3 (Te $3d_{5/2}$), and it is associated with an oxidized component formed during the material's exposure to ambient conditions for manipulation and transportation.

To produce SnTe-based composites, the SnTe molecular precursor was combined with different amounts of $Cu_{1.5}Te$ nanocrystals dispersed in OAm (Figures 2a and S1, see the

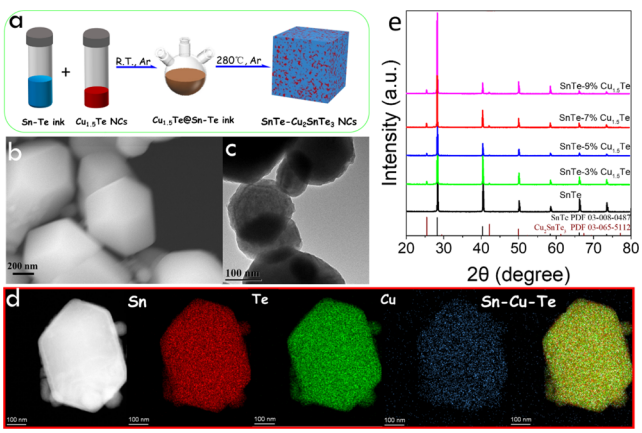

Figure 2. (a) Schematic diagram of the engineering of SnTe−Cu_2SnTe_3 composites from a combination of the Sn−Te ink (blue) and a colloidal dispersion of $Cu_{1.5}Te$ nanoparticles (red). (b) SEM and (c) TEM image of SnTe−7% $Cu_{1.5}Te$ composite, (d) HAADF image and EDX elemental maps of Sn, Te, and Cu. (e) XRD patterns of the different composites.

Supporting Information for details on the synthesis of $Cu_{1.5}Te$). The obtained solution was decomposed at 280 °C. All the synthesized SnTe-*y*% $Cu_{1.5}Te$ composite powders displayed similar particle morphologies as the pristine SnTe particles. Figure 2b,c displays representative SEM and TEM images of the SnTe−7% $Cu_{1.5}Te$ composite. EDX mapping shows a uniform distribution of Cu, Sn, and Te, denoting the presence of some amount of Cu within the SnTe particles (Figure 2d). Figure 2e shows the XRD pattern of the different samples. The main diffraction peaks can be indexed as the rock-salt structure of SnTe (PDF 00-008-0487). Besides, additional XRD peaks are visible at 25.5 and 42.2° and correspond to the (111) and (220) family planes of the Cu_2SnTe_3 cubic phase (PDF 03-065-5112). No $Cu_{2-x}Te$ phase could be detected by XRD. The disappearance of the $Cu_{1.5}Te$ phase, the ubiquitous presence of Cu, and the appearance of a small amount of Cu_2SnTe_3 indicate the Cu diffusion within SnTe particles and the segregation of a ternary Cu−Sn−Te phase from the partial reaction of Sn and Te precursors with $Cu_{1.5}Te$. The SnTe XRD peak positions within the SnTe-*y*% $Cu_{1.5}Te$ composite are influenced by the presence of Cu, further evidencing the presence of Cu within the SnTe lattice. As observed in Figure S4, with the increase of the $Cu_{1.5}Te$ amount within the initial precursor, the (200) XRD peak initially shifts to notably lower angles, probably due to the presence of interstitial Cu within SnTe, and then slightly returns toward its initial position because of the segregation of the Cu_2SnTe_3 phase, decreasing the amount of Cu within the SnTe lattice.

As schematized in Figure 3a, to evaluate the TE properties of SnTe and SnTe-*y*% $Cu_{1.5}Te$, the annealed powders (853 K for 120 min under Ar, see details in the Supporting Information) were sintered into disk-shaped pellets by hot pressing under 40 M uniaxial pressure at 773 K for 5 min in an argon-filled glovebox (see details in the Supporting Information). The relative densities of the sintered pellets determined by the Archimedes method were all above 97% (Table S2, Supporting Information). Figure 3b shows the XRD patterns of sintered SnTe and SnTe-*y*% $Cu_{1.5}Te$ (y = 3, 5, 7, and 9%) pellets. The Cu_2SnTe_3 secondary phase can be detected only when the precursor $Cu_{1.5}Te$ concentration is ≥5%. As for the sintered powder, when increasing the precursor $Cu_{1.5}Te$ concentration, the SnTe XRD patterns show first a strong shift to lower diffraction angles that it is partially recovered at higher $Cu_{1.5}Te$ concentrations. We assign the XRD peak shift toward a higher angle position with the precursor $Cu_{1.5}Te$ content from 7 to 9% with the segregation of the Cu_2SnTe_3 phase, reducing the amount of Cu within the SnTe lattice.

To visualize the internal microstructure and morphology of the sintered samples, representative SEM images of the fractured pellets are displayed in Figures 3c,d and S5−S7. The cross-sectional SEM micrographs of SnTe exhibit small grains. Compared with pristine SnTe, the presence of $Cu_{1.5}Te$ in the thermally decomposed precursor solution boosts the crystal growth during the thermal processes, increasing the crystal domain size of the final SnTe-*y*% $Cu_{1.5}Te$ composites by more than one order of magnitude. The large grain growth is mainly assigned to the hot-pressing sintering process instead of the annealing process (Figure S6c,e). The enhanced crystal growth is related to the low melting point of the Cu_2SnTe_3 phase formed at 680 K.[87] As the melting point of Cu_2SnTe_3 is below that used during hot pressing, the Cu_2SnTe_3 phase melts during the process and acts as a solvent, promoting the diffusion of Sn and Te atoms and promoting the SnTe grain growth to micron-sized grains.[74] No preferential growth or orientation of the crystals within the pellets was observed either by SEM analysis or XRD analysis (Figure S7), which points toward a material having anisotropic properties.

https://doi.org/10.1021/acsami.3c00625
ACS Appl. Mater. Interfaces 2023, 15, 23380−23389

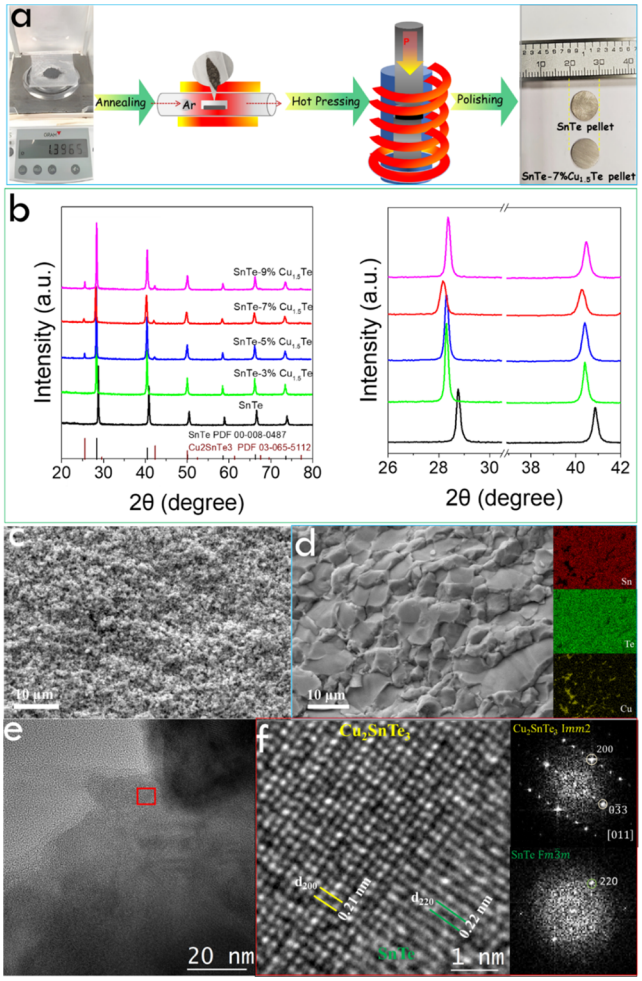

Figure 3. (a) Schematic illustration of the hot pressing of the annealed composites into a pellet. (b) XRD patterns of sintered SnTe-y% $Cu_{1.5}Te$ pellets (y = 0, 3, 5, 7, and 9%) and enlarged (200) and (220) peaks. (c) Cross-sectional SEM image of the sintered SnTe pellet. (d) Cross-section SEM image of the sintered SnTe−7% $Cu_{1.5}Te$ pellet and corresponding EDX maps of Sn, Te, and Cu. (e) HRTEM image of SnTe−7% $Cu_{1.5}Te$ pellet. (f) HRTEM image of the red area in (e), and FFT from SnTe and Cu_2SnTe_3 different phase regions, respectively.

EDX elemental maps show a homogeneous distribution of Sn, Te, and Cu throughout the whole pellet at a low (3%) $Cu_{1.5}Te$ concentration. In contrast, Cu-rich areas are found in the composites obtained from larger amounts of precursor $Cu_{1.5}Te$, 5, 7, and 9%. This observation is consistent with the XRD results. Taking into account the XRD data, we associate the local Cu accumulation in the SnTe matrix with the presence of nanoprecipitates of the Cu_2SnTe_3 phase. The presence of Cu_2SnTe_3 crystal domains within the composites was further confirmed by HRTEM. As shown in Figure 3e,f, a d-spacing of 0.22 nm is assigned to the (220) planes of the SnTe matrix. Besides, Cu_2SnTe_3 nanodomains are identified with a d-spacing of 0.21 nm, which corresponds to the (200) plane of the Cu_2SnTe_3 phase. The size of the Cu_2SnTe_3 nanodomains observed on the HRTEM image is ca. 10 nm (Figure S8a,b). HAADF-EDX maps show a relatively uniform distribution of Sn and Te elements, while some Cu-rich areas are evident (Figure S8c).

Figures 4a and S9a display the electrical conductivity (σ) of both SnTe and SnTe-y% $Cu_{1.5}Te$ samples to monotonically decrease with temperature, as it corresponds with a degenerated semiconductor behavior. For SnTe, the electrical conductivity is about 3.4×10^5 S m^{-1} at room temperature, which is consistent with our previous report.[73] The electrical conductivity of all the composites is higher than that of SnTe in the whole temperature range, and it increases when increasing the $Cu_{1.5}Te$ concentration within the precursor. The increased electrical conductivity is in part associated with the presence of Cu within the SnTe structure, acting as an electron acceptor. At high enough $Cu_{1.5}Te$ concentrations, the formation of the Cu_2SnTe_3 phase may also contribute to the charge transport by accepting electrons or facilitating the charge transport at the grain boundary. Notice in this regard that Cu_2SnTe_3 is generally regarded as a low-carrier density semimetal.[88] At the same time, the large grains generated in the presence of the Cu_2SnTe_3 phase also contribute to the electrical conductivity but have little effect on the Seebeck coefficient.[89]

Table S3 displays the Hall carrier concentration (η_H) and mobility (μ_H) of the different samples at room temperature. With increasing the precursor $Cu_{1.5}Te$ content, a clear increase of the charge carrier concentration and a simultaneous reduction of the mobility are obtained. η_H values increase almost an order of magnitude, from 3.2×10^{20} cm^{-3} for SnTe to 1.8×10^{21} cm^{-3} for SnTe−9% $Cu_{1.5}Te$, while the mobility decreases a factor of 3, from 69.3 cm^2 V^{-1} s^{-1} for SnTe to 27.8 cm^2 V^{-1} s^{-1} for SnTe−9% $Cu_{1.5}Te$.

Positive Seebeck coefficients monotonously increasing with temperature were obtained for all the samples in the whole temperature range measured, consistent with a p-type semiconductor behavior. S was higher for SnTe than for the different composites in the low temperature range, consistent with the charge carrier concentrations. However, in the highest temperature range tested, 700−800 K, the composite S exceeded that of pristine SnTe (Figures 4b and S9b).[42] This reversal is attributed to the decreased Sn vacancies caused by the incorporation of Cu,[90] whose anomalous behavior has been previously reported in SnTe-based TE materials.[42,43,74,91] Figure 4c displays the Pisarenko plot of the Seebeck coefficient as a function of the hole carrier concentration calculated using a two-valence-band model.[12] The values obtained for all the samples follow the proper trend and are also consistent with previously reported data.

Overall, the power factors (PF, $S^2\sigma$) of all the SnTe-y% $Cu_{1.5}Te$ composites were significantly larger than those of SnTe, especially in the medium−high temperature range tested, 600−800 K (Figures 4d and S9c). The highest power factors were obtained for the SnTe-7% $Cu_{1.5}Te$ composite, reaching 3.63 mW m^{-1} K^{-2} at 823 K, which is in the high-value range of the previously reported PF values for SnTe (Figure 4e and Table S4).

As shown in Figures 5a and S9d, the total room temperature thermal conductivity (κ_{tot}) of SnTe and the SnTe-y% $Cu_{1.5}Te$ composites was relatively high, around 6 W m^{-1} K^{-1}. It monotonously decreased with temperature for all the samples, down to 3.4 W m^{-1} K^{-1} at 823 K for SnTe and 2.8 W m^{-1} K^{-1} for SnTe−7%$Cu_{1.5}Te$. κ_{tot} decreased with the precursor $Cu_{1.5}Te$ content at small $Cu_{1.5}Te$ concentrations but returned toward the pristine SnTe values at the highest $Cu_{1.5}Te$ loadings tested. This complex evolution is related to the different contributions of the electron (κ_e) and lattice (κ_L) thermal conductivities. κ_e was calculated from the Wiedemann−Franz equation, $\kappa_e = L\sigma T$, using the Lorenz number (L) estimated

https://doi.org/10.1021/acsami.3c00625
ACS Appl. Mater. Interfaces 2023, 15, 23380−23389

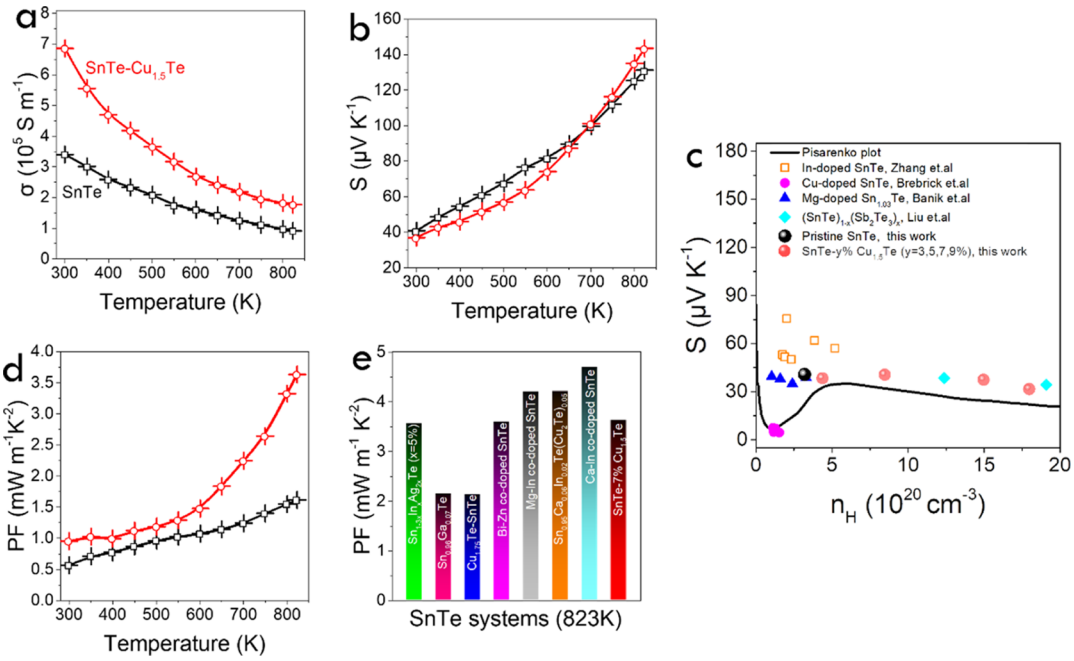

Figure 4. (a,b) Temperature dependence of (a) electrical conductivity, σ. (b) Seebeck coefficient, S. (c) Room temperature Seebeck coefficient (S) as a function of Hall carrier concentrations (n_H). The solid line is the room temperature theoretical Pisarenko plot calculated using a two-valence-band model. Previously reported In-doped SnTe,[12] Cu-doped SnTe,[92] Mg-doped $Sn_{1.03}Te$,[93] and $(SnTe)_{1-x}(Sb_2Te_3)_x$[94] are listed for comparison. (d) Power factor, $S^2\sigma$, PF for the pristine SnTe and SnTe-7% $Cu_{1.5}Te$. (e) Comparison of power factor with different state-of-the-art SnTe-based TE systems: $Sn_{1-3x}In_xAg_{2x}Te$ (x = 5%),[52] $Sn_{0.96}Ga_{0.07}Te$,[95] $Cu_{1.75}Te$-SnTe,[42] Bi− Zn co-doped SnTe,[96] Mg−In co-doped SnTe,[97] $Sn_{0.95}Ca_{0.06}In_{0.02}Te(Cu_2Te)_{0.05}$,[40] and Ca−In co-doped SnTe.[98]

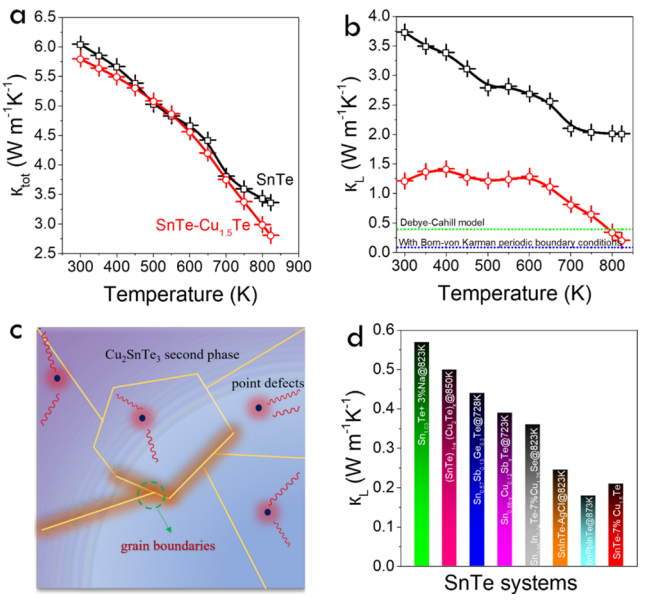

Figure 5. Temperature dependence of (a) total thermal conductivity, κ_{total}; (b) lattice thermal conductivity, κ_L, for SnTe and SnTe-7% $Cu_{1.5}Te$. (c) Schematic diagram of various possible phonon scattering and κ_L. (d) Comparison of the lowest κ_L over test temperature with previously reported SnTe-based systems: $Sn_{0.88-y}Cu_{0.12}Sb_yTe$,[103] $Sn_{0.85}Sb_{0.15}Te$,[104] $Sn_{0.96}In_{0.04}Te$−7%$Cu_{1.75}Se$,[34] $Sn_{0.96}Pb_{0.01}In_{0.03}Te$,[81] $(Sn_{0.985}In_{0.015}Te)_{0.90}(AgCl)_{0.10}$,[55] $Sn_{1.03}Te$ + 3% Na,[26] Ag-doped SnTe,[54] $(SnTe)_{1-x}(Cu_2Te)_x$,[43] and $Sn_{0.57}Sb_{0.13}Ge_{0.3}Te$.[105]

from the measured Seebeck coefficient, $L = 1.5 + \exp[-|S|/116] \times 10^{-8}$.[99,100] The obtained L values and κ_e can be found in Figure S9e,f. κ_L was evaluated by subtracting κ_e from κ_{tot} (Figure S9g). Significantly lower κ_L values were obtained for the composite materials compared with SnTe, and a clear decrease of κ_L was obtained when increasing the precursor $Cu_{1.5}Te$ content. The lowest κ_L, 0.21 W m^{-1} K^{-1}, was obtained for SnTe− 9% $Cu_{1.5}Te$. This value was lower than the amorphous limit of SnTe as calculated from the Debye−Cahill model (≈0.4 W m^{-1} K^{-1}).[101] Meanwhile, this low κ_L was still higher than the Born-von Karman periodic boundary conditions (Figure 5b).[102] The low κ_L obtained for the SnTe-y% $Cu_{1.5}Te$ composites is related to the multiscale scattering centers present in these samples, including the Cu impurities within the SnTe crystals, SnTe/Cu_2SnTe_3 nanoscale interphases, and SnTe/SnTe grain boundaries (Figure 5c). Notice that the compositional inhomogeneities can be particularly effective in scattering wide-frequency phonons.[55] In this same direction, the slight lattice mismatch between the cubic SnTe (a = 6.303 Å) and Cu_2SnTe_3 (a = 6.047 Å) results in a lattice distortion that can introduce strain fields within the SnTe, further hampering phonon propagation.[53] Besides, above 600 K, a clear decrease of κ_L is obtained for the samples containing the largest amounts of precursor $Cu_{1.5}Te$, and it is associated with the melting of the Cu_2SnTe_3 phase at the grain boundaries. As can be seen from Figure 5d, SnTe-y% $Cu_{1.5}Te$ composites are characterized by relatively low κ_L values compared with previous reports. Similar ultralow κ_L values, down to 0.18 W m^{-1} K^{-1}, were achieved for hydrothermally synthesized $Sn_{0.96}Pb_{0.01}In_{0.03}Te$ samples and were associated with reduced grain sizes, scattering by nanoparticles and point defects.[81]

Overall, the enhanced PF and reduced κ_L obtained for the SnTe-y% $Cu_{1.5}Te$ composites resulted in significantly increased ZT values with respect to SnTe, particularly in the medium/high-temperature range, reaching a maximum of 1.04 at 823 K for the SnTe−7% $Cu_{1.5}Te$ nanocomposite (Figures 6a and

https://doi.org/10.1021/acsami.3c00625
ACS Appl. Mater. Interfaces 2023, 15, 23380−23389

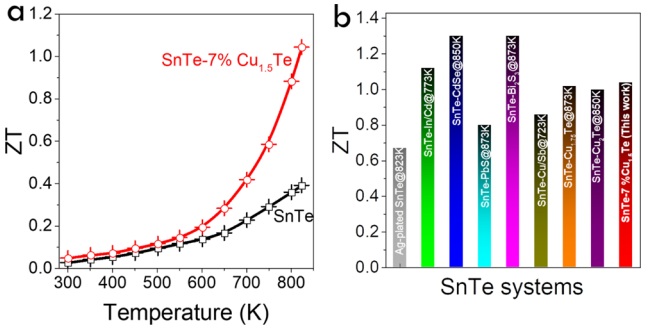

Figure 6. Temperature dependence of (a) TE figure of merit ZT values for SnTe-7% $Cu_{1.5}Te$. (b) Comparison of peak ZT values for SnTe-based TE materials in this work and previous reports, including solution-based preparation such as Ag,[54] In/Cd,[82] CdSe,[73] PbS,[74] Bi_2S_3,[106] Sb_2Se_3,[94] and Cu-incorporation solid phase sintering of Cu/Sb,[103] $Cu_{1.75}Te$,[42] and Cu_2Te.[43]

S9h).[82] This high ZT represents a 170% enhancement compared with pristine SnTe. Figure 6b shows a comparison of the ZT values obtained for the SnTe-7% $Cu_{1.5}Te$ at 823 K with those previously reported for SnTe-based materials, including solution-based preparation, such as Ag,[54] In/Cd,[82] CdSe,[73] PbS,[74] Bi_2S_3,[106] Sb_2Se_3,[94] and Cu-incorporation solid phase sintering of Cu/Sb,[103] $Cu_{1.75}Te$,[42] and Cu_2Te.[43] The composites reported here display relatively large ZT values in this temperature range. The ZT values of SnTe-based TE materials reported in recent years are summarized in Table S4. As shown in Figure S10, measurements from multiple samples confirmed the reproducibility of the obtained values. Besides, thermal gravimetric analysis (TGA) of the composites confirmed their excellent thermal stability against a loss of chalcogen or chalcogenide phases (Figure S11). Actually, compared with the pristine SnTe sample, the SnTe-7% $Cu_{1.5}Te$ composite exhibits enhanced stability against the slight volatilization of Sn observed in SnTe.[51] On the other hand, the SnTe-7% $Cu_{1.5}Te$ composite presented a slightly lower hardness than the SnTe sample (Figure S12).

CONCLUSIONS

In summary, a Sn−Te inorganic molecular precursor ink was prepared by dissolving a Sn salt and Te in a hydrazine- and thiol-free solvent system. The thermal decomposition of this precursor at 280 °C resulted in the formation of pure SnTe. The SnTe precursor ink was combined with a colloidal suspension of $Cu_{1.5}Te$ nanocrystals to produce SnTe−Cu_2SnTe_3 nanocomposites. The presence of $Cu_{1.5}Te$ in the precursor solution enhanced the growth of the SnTe crystal domains due to the formation of the low melting point phase Cu_2SnTe_3. The SnTe−Cu_2SnTe_3 nanocomposites showed significantly larger electrical conductivities than SnTe, which was in part related to the Cu doping with the SnTe crystals acting as acceptors. At the same time, slightly larger Seebeck coefficients were also obtained with the introduction of $Cu_{1.5}Te$ within the precursor solution, particularly in the medium/high-temperature range. Thus, overall higher PFs up to 3.63 mW m^{-1} K^{-2} were obtained for the SnTe−Cu_2SnTe_3 composites. Besides, the presence of Cu ions within the SnTe crystal and the abundant Cu_2SnTe_3 nanoprecipitates significantly reduced the lattice thermal conductivity, down to 0.21 W m^{-1} K^{-1}. Ultimately, a ZT value of 1.04 was achieved at 823 K due to the simultaneous improvement of electrical and thermal transport properties. The strategy reported here not only provides an alternative approach for the preparation of functional metal chalcogenides and related nanocomposites from easily processable and scalable molecular precursor inks but also provides a meaningful perspective for developing high-performance lead-free medium/high-temperature TE materials.

ASSOCIATED CONTENT

Supporting Information

The Supporting Information is available free of charge at https://pubs.acs.org/doi/10.1021/acsami.3c00625.

Experimental details; comparison of performance; and additional SEM, XRD, EDX, HRTEM, TGA, hardness, and transport property characterization (PDF)

AUTHOR INFORMATION

Corresponding Authors

Maria Ibáñez − *Institute of Science and Technology Austria (ISTA), Klosterneuburg 3400, Austria;* orcid.org/0000-0001-5013-2843; Email: mibanez@ist.ac.at

Andreu Cabot − *Catalonia Institute for Energy Research—IREC, Barcelona 08930, Spain; ICREA, Barcelona 08010 Catalonia, Spain;* orcid.org/0000-0002-7533-3251; Email: acabot@irec.cat

Authors

Bingfei Nan − *Catalonia Institute for Energy Research—IREC, Barcelona 08930, Spain; Universitat de Barcelona, Barcelona 08028, Spain*

Xuan Song − *The State Key Laboratory of Chemical Engineering, Department of Chemical Engineering, Tsinghua University, Beijing 100084, China*

Cheng Chang − *Institute of Science and Technology Austria (ISTA), Klosterneuburg 3400, Austria; School of Materials Science and Engineering, Beihang University, Beijing 100191, China*

Ke Xiao − *Catalonia Institute for Energy Research—IREC, Barcelona 08930, Spain; Universitat de Barcelona, Barcelona 08028, Spain*

Yu Zhang − *Department of Materials Science and Engineering, Pennsylvania State University, State College, Pennsylvania 16802, United States*

Linlin Yang − *Catalonia Institute for Energy Research—IREC, Barcelona 08930, Spain; Universitat de Barcelona, Barcelona 08028, Spain*

Sharona Horta − *Institute of Science and Technology Austria (ISTA), Klosterneuburg 3400, Austria*

Junshan Li − *Institute of Advanced Study, Chengdu University, Chengdu 610106, China;* orcid.org/0000-0002-1482-1972

Khak Ho Lim − *Institute of Zhejiang University—Quzhou, Quzhou 324000 Zhejiang, P. R. China; College of Chemical and Biological Engineering, Zhejiang University, Hangzhou 310007 Zhejiang, P. R. China*

Complete contact information is available at: https://pubs.acs.org/10.1021/acsami.3c00625

Funding

Open Access is funded by the Austrian Science Fund (FWF).

Notes

The authors declare no competing financial interest.

■ ACKNOWLEDGMENTS

We thank Generalitat de Catalunya AGAUR—2021 SGR 01581 for financial support. B.F.N., K.X., and L.L.Y. thank the China Scholarship Council (CSC) for the scholarship support. C.C. acknowledges funding from the FWF "Lise Meitner Fellowship" grant agreement M 2889-N. J.S.L is grateful to the Science and Technology Department of Sichuan Province for the project no. 22NSFSC0966. K.H.L. was supported by the Institute of Zhejiang University-Quzhou (IZQ2021RCZX003). M.I. acknowledges the financial support from IST Austria.

■ REFERENCES

(1) Tan, G.; Zhao, L.-D.; Kanatzidis, M. G. Rationally Designing High-Performance Bulk Thermoelectric Materials. *Chem. Rev.* **2016**, *116*, 12123−12149.
(2) Poudel, B.; Hao, Q.; Ma, Y.; Lan, Y.; Minnich, A.; Yu, B.; Yan, X.; Wang, D.; Muto, A.; Vashaee, D.; Chen, X.; Liu, J.; Dresselhaus, M. S.; Chen, G.; Ren, Z. High-Thermoelectric Performance of Nanostructured Bismuth Antimony Telluride Bulk Alloys. *Science* **2008**, *320*, 634−638.
(3) He, J.; Tritt, T. M. Advances in thermoelectric materials research: Looking back and moving forward. *Science* **2017**, *357*, 9.
(4) Liu, Y.; Zhang, Y.; Ortega, S.; Ibáñez, M.; Lim, K. H.; Grau-Carbonell, A.; Martí-Sánchez, S.; Ng, K. M.; Arbiol, J.; Kovalenko, M. V.; Cadavid, D.; Cabot, A. Crystallographically Textured Nanomaterials Produced from the Liquid Phase Sintering of $Bi_xSb_{2-x}Te_3$ Nanocrystal Building Blocks. *Nano Lett.* **2018**, *18*, 2557−2563.
(5) Liu, Y.; Zhang, Y.; Lim, K. H.; Ibáñez, M.; Ortega, S.; Li, M.; David, J.; Martí-Sánchez, S.; Ng, K. M.; Arbiol, J.; Kovalenko, M. V.; Cadavid, D.; Cabot, A. High Thermoelectric Performance in Crystallographically Textured n-Type $Bi_2Te_{3-x}Se_x$ Produced from Asymmetric Colloidal Nanocrystals. *ACS Nano* **2018**, *12*, 7174−7184.
(6) Zhang, Y.; Xing, C.; Liu, Y.; Li, M.; Xiao, K.; Guardia, P.; Lee, S.; Han, X.; Ostovari Moghaddam, A.; Josep Roa, J.; Arbiol, J.; Ibáñez, M.; Pan, K.; Prato, M.; Xie, Y.; Cabot, A. Influence of copper telluride nanodomains on the transport properties of n-type bismuth telluride. *Chem. Eng. J.* **2021**, *418*, 129374.
(7) Zhang, Y.; Liu, Y.; Calcabrini, M.; Xing, C. C.; Han, X.; Arbiol, J.; Cadavid, D.; Ibanez, M.; Cabot, A. Bismuth telluride-copper telluride nanocomposites from heterostructured building blocks. *J. Mater. Chem. C* **2020**, *8*, 14092−14099.
(8) Zhou, C. J.; Chung, I. Nanoscale defect structures advancing high performance n-type PbSe thermoelectrics. *Coord. Chem. Rev.* **2020**, *421*, 213437.
(9) Sun, J.; Zhang, Y.; Fan, Y.; Tang, X.; Tan, G. Strategies for boosting thermoelectric performance of PbSe: A review. *Chem. Eng. J.* **2022**, *431*, 133699.
(10) Heremans, J. P.; Jovovic, V.; Toberer, E. S.; Saramat, A.; Kurosaki, K.; Charoenphakdee, A.; Yamanaka, S.; Snyder, G. J. Enhancement of Thermoelectric Efficiency in PbTe by Distortion of the Electronic Density of States. *Science* **2008**, *321*, 554−557.
(11) Xiao, Y.; Wu, H.; Shi, H.; Xu, L.; Zhu, Y.; Qin, Y.; Peng, G.; Zhang, Y.; Ge, Z.-H.; Ding, X.; Zhao, L.-D. High-Ranged ZT Value Promotes Thermoelectric Cooling and Power Generation in n-Type PbTe. *Adv. Electron. Mater.* **2022**, *12*, 2200204.
(12) Zhang, Q.; Liao, B.; Lan, Y.; Lukas, K.; Liu, W.; Esfarjani, K.; Opeil, C.; Broido, D.; Chen, G.; Ren, Z. High thermoelectric performance by resonant dopant indium in nanostructured SnTe. *Proc. Natl. Acad. Sci. U.S.A.* **2013**, *110*, 13261−13266.
(13) Li, W.; Zheng, L.; Ge, B.; Lin, S.; Zhang, X.; Chen, Z.; Chang, Y.; Pei, Y. Promoting SnTe as an Eco-Friendly Solution for p-PbTe Thermoelectric via Band Convergence and Interstitial Defects. *Adv. Mater.* **2017**, *29*, 1605887.
(14) Zhang, Y.; Sun, J.; Shuai, J.; Tang, X.; Tan, G. Lead-free SnTe-based compounds as advanced thermoelectrics. *Mater. Today Phys.* **2021**, *19*, 100405.
(15) Moshwan, R.; Yang, L.; Zou, J.; Chen, Z.-G. Eco-Friendly SnTe Thermoelectric Materials: Progress and Future Challenges. *Adv. Funct. Mater.* **2017**, *27*, 1703278.
(16) Shenoy, U. S.; Bhat, D. K. Molybdenum as a versatile dopant in SnTe: a promising material for thermoelectric application. *Energy Adv.* **2022**, *1*, 9−14.
(17) Ma, Z.; Xu, T.; Li, W.; Cheng, Y.; Li, J.; Wei, Y.; Jiang, Q.; Luo, Y.; Yang, J. High Thermoelectric Performance SnTe with a Segregated and Percolated Structure. *ACS Appl. Mater. Interfaces* **2022**, *14*, 9192−9202.
(18) Shenoy, U. S.; Goutham, K. D.; Bhat, D. K. A case of perfect convergence of light and heavy hole valence bands in SnTe: the role of Ge and Zn co-dopants. *Mater. Adv.* **2022**, *3*, 5941−5946.
(19) Hong, T.; Guo, C.; Wang, D.; Qin, B.; Chang, C.; Gao, X.; Zhao, L.-D. Enhanced thermoelectric performance in SnTe due to the energy filtering effect introduced by Bi_2O_3. *Mater. Today Energy* **2022**, *25*, 100985.
(20) Li, S.; Zhang, J.; Liu, D.; Wang, Y.; Zhang, J. Improving thermoelectric performance by constructing a SnTe/ZnO core−shell structure. *RSC Adv.* **2022**, *12*, 23074−23082.
(21) Pathak, R.; Sarkar, D.; Biswas, K. Enhanced Band Convergence and Ultra-Low Thermal Conductivity Lead to High Thermoelectric Performance in SnTe. *Angew. Chem., Int. Ed.* **2021**, *60*, 17686−17692.
(22) Shenoy, U. S.; Bhat, D. K. Improving the ZT of SnTe using electronic structure engineering: unusual behavior of Bi dopant in the presence of Pb as a co-dopant. *Mater. Adv.* **2021**, *2*, 6267−6271.
(23) Shenoy, U. S.; Goutham, K. D.; Bhat, D. K. Resonance states and hyperconvergence induced by tungsten doping in SnTe: Multiband transport leading to a propitious thermoelectric material. *J. Alloys Compd.* **2022**, *905*, 164146.
(24) Bhat, D. K.; Shenoy, U. S. SnTe thermoelectrics: Dual step approach for enhanced performance. *J. Alloys Compd.* **2020**, *834*, 155181.
(25) Shenoy, U. S.; Bhat, D. K. Vanadium: A Protean Dopant in SnTe for Augmenting Its Thermoelectric Performance. *ACS Sustainable Chem. Eng.* **2021**, *9*, 13033−13038.
(26) Abbas, A.; Nisar, M.; Zheng, Z. H.; Li, F.; Jabar, B.; Liang, G.; Fan, P.; Chen, Y.-X. Achieving High Thermoelectric Performance of Eco-Friendly SnTe-Based Materials by Selective Alloying and Defect Modulation. *ACS Appl. Mater. Interfaces* **2022**, *14*, 25802−25811.
(27) Qi, X.; Huang, Y.; Wu, D.; Jiang, B.; Zhu, B.; Xu, X.; Feng, J.; Jia, B.; Shu, Z.; He, J. Eutectoid nano-precipitates inducing remarkably enhanced thermoelectric performance in $(Sn_{1-x}Cd_xTe)_{1-y}(Cu_2Te)_y$. *J. Mater. Chem. A* **2020**, *8*, 2798−2808.
(28) Tan, G.; Shi, F.; Hao, S.; Chi, H.; Zhao, L.-D.; Uher, C.; Wolverton, C.; Dravid, V. P.; Kanatzidis, M. G. Codoping in SnTe: Enhancement of Thermoelectric Performance through Synergy of Resonance Levels and Band Convergence. *J. Am. Chem. Soc.* **2015**, *137*, 5100−5112.
(29) Ma, Z.; Wang, C.; Chen, Y.; Li, L.; Li, S.; Wang, J.; Zhao, H. Ultra-high thermoelectric performance in SnTe by the integration of several optimization strategies. *Mater. Today Phys.* **2021**, *17*, 100350.
(30) Wang, J.; Yu, Y.; He, J.; Wang, J.; Ma, B.; Chao, X.; Yang, Z.; Wu, D. Synergy of Valence Band Modulation and Grain Boundary Engineering Leading to Improved Thermoelectric Performance in SnTe. *ACS Appl. Energy Mater.* **2021**, *4*, 14608−14617.
(31) Li, M. R.; Ying, P. Z.; Du, Z. L.; Liu, X. L.; Li, X.; Fang, T.; Cui, J. L. Improved Thermoelectric Performance of P-type SnTe through Synergistic Engineering of Electronic and Phonon Transports. *ACS Appl. Mater. Interfaces* **2022**, *14*, 8171−8178.
(32) Tan, G.; Zeier, W. G.; Shi, F.; Wang, P.; Snyder, G. J.; Dravid, V. P.; Kanatzidis, M. G. High Thermoelectric Performance SnTe−In_2Te_3 Solid Solutions Enabled by Resonant Levels and Strong Vacancy Phonon Scattering. *Chem. Mater.* **2015**, *27*, 7801−7811.
(33) Gao, B.; Tang, J.; Meng, F.; Li, W. Band manipulation for high thermoelectric performance in SnTe through heavy CdSe-alloying. *J Materiomics* **2019**, *5*, 111−117.
(34) Li, D.; Ming, H. W.; Li, J. M.; Zhang, J.; Qin, X. Y.; Xu, W. High Thermoelectric Performance of SnTe via In Doping and

$Cu_{1.75}Se$ Nanostructuring Approach. *ACS Appl. Energy Mater.* **2019**, *2*, 8966−8973.
(35) Li, X.; Liu, J.; Li, S.; Zhang, J.; Li, D.; Xu, R.; Zhang, Q.; Zhang, X.; Xu, B.; Zhang, Y.; Xu, F.; Tang, G. Synergistic band convergence and endotaxial nanostructuring: Achieving ultralow lattice thermal conductivity and high figure of merit in eco-friendly SnTe. *Nano Energy* **2020**, *67*, 104261.
(36) He, S.; Zhang, F.; Li, R.; Gan, L.; Tan, X.; Zhu, J.; Ang, R. Synergistic band modulation and precipitates: Achieving high quality factor in SnTe. *Appl. Phys. Lett.* **2023**, *122*, 072102.
(37) Tan, G.; Shi, F.; Sun, H.; Zhao, L.-D.; Uher, C.; Dravid, V. P.; Kanatzidis, M. G. SnTe−$AgBiTe_2$ as an efficient thermoelectric material with low thermal conductivity. *J. Mater. Chem. A* **2014**, *2*, 20849−20854.
(38) Ma, Z.; Wang, C.; Lei, J.; Zhang, D.; Chen, Y.; Wang, J.; Cheng, Z.; Wang, Y. High Thermoelectric Performance of SnTe by the Synergistic Effect of Alloy Nanoparticles with Elemental Elements. *ACS Appl. Mater. Interfaces* **2019**, *2*, 7354−7363.
(39) Xu, H.; Wan, H.; Xu, R.; Hu, Z.; Liang, X.; Li, Z.; Song, J. Enhancing the thermoelectric performance of SnTe-$CuSbSe_2$ with an ultra-low lattice thermal conductivity. *J. Mater. Chem. A* **2023**, *11*, 4310−4318.
(40) Hussain, T.; Li, X.; Danish, M. H.; Rehman, M. U.; Zhang, J.; Li, D.; Chen, G.; Tang, G. Realizing high thermoelectric performance in eco-friendly SnTe via synergistic resonance levels, band convergence and endotaxial nanostructuring with Cu_2Te. *Nano Energy* **2020**, *73*, 104832.
(41) Song, S.; Lo, C.-W. T.; Aminzare, M.; Tseng, Y.-C.; Valiyaveettil, S. M.; Mozharivskyj, Y. Enhancing the thermoelectric performance of $Sn_{0.5}Ge_{0.5}Te$ via doping with Sb/Bi and alloying with Cu_2Te: Optimization of transport properties and thermal conductivities. *Dalton Trans.* **2020**, *49*, 6135−6144.
(42) Jiang, Q.; Hu, H.; Yang, J.; Xin, J.; Li, S.; Viola, G.; Yan, H. High Thermoelectric Performance in SnTe Nanocomposites with All-Scale Hierarchical Structures. *ACS Appl. Mater. Interfaces* **2020**, *12*, 23102−23109.
(43) Pei, Y.; Zheng, L.; Li, W.; Lin, S.; Chen, Z.; Wang, Y.; Xu, X.; Yu, H.; Chen, Y.; Ge, B. Interstitial Point Defect Scattering Contributing to High Thermoelectric Performance in SnTe. *Adv. Electron. Mater.* **2016**, *2*, 1600019.
(44) Tang, J.; Gao, B.; Lin, S. Q.; Li, J.; Chen, Z. W.; Xiong, F.; Li, W.; Chen, Y.; Pei, Y. Z. Manipulation of Band Structure and Interstitial Defects for Improving Thermoelectric SnTe. *Adv. Funct. Mater.* **2018**, *28*, 1803586.
(45) Sarkar, D.; Ghosh, T.; Banik, A.; Roychowdhury, S.; Sanyal, D.; Biswas, K. Highly Converged Valence Bands and Ultralow Lattice Thermal Conductivity for High-Performance SnTe Thermoelectrics. *Angew. Chem., Int. Ed.* **2020**, *59*, 11115−11122.
(46) Shenoy, U. S.; Bhat, D. K. Selective co-doping improves the thermoelectric performance of SnTe: An outcome of electronic structure engineering. *J. Alloys Compd.* **2022**, *892*, 162221.
(47) Zhang, T.; Pan, W.; Ning, S.; Qi, N.; Chen, Z.; Su, X.; Tang, X. Vacancy Manipulation Induced Optimal Carrier Concentration, Band Convergence and Low Lattice Thermal Conductivity in Nano-Crystalline SnTe Yielding Superior Thermoelectric Performance. *Adv. Funct. Mater.* **2022**, *33*, 2213761.
(48) Yan, X.; Zheng, S.; Zhou, Z.; Wu, H.; Zhang, B.; Huang, Y.; Lu, X.; Han, G.; Wang, G.; Zhou, X. Melt-spun $Sn_{1-x-y}Sb_xMn_yTe$ with unique multiscale microstructures approaching exceptional average thermoelectric zT. *Nano Energy* **2021**, *84*, 105879.
(49) Su, H.; Han, Y.; Zhou, M.; Huang, R.; Miao, Z.; Li, L. One-step fabrication of a bulk SnTe thermoelectric material with excellent performance through self-propagating high-temperature synthesis under a high-gravity field. *Mater. Chem. Front.* **2022**, *6*, 2175−2183.
(50) Bhat, D. K.; Shenoy, U. S. Zn: a versatile resonant dopant for SnTe thermoelectrics. *Mater. Today Phys.* **2019**, *11*, 100158.
(51) Tian, B.-Z.; Chen, J.; Jiang, X.-P.; Tang, J.; Zhou, D.-L.; Sun, Q.; Yang, L.; Chen, Z.-G. Enhanced Thermoelectric Performance of SnTe-Based Materials via Interface Engineering. *ACS Appl. Mater. Interfaces* **2021**, *13*, 50057−50064.
(52) Moshwan, R.; Liu, W.-D.; Shi, X.-L.; Sun, Q.; Gao, H.; Wang, Y.-P.; Zou, J.; Chen, Z.-G. Outstanding thermoelectric properties of solvothermal-synthesized $Sn_{1-3x}In_xAg_{2x}Te$ micro-crystals through defect engineering and band tuning. *J. Mater. Chem. A* **2020**, *8*, 3978−3987.
(53) Moshwan, R.; Shi, X.-L.; Liu, W.-D.; Wang, Y.; Xu, S.; Zou, J.; Chen, Z.-G. Enhancing Thermoelectric Properties of InTe Nano-precipitate-Embedded $Sn_{1-x}In_xTe$ Microcrystals through Anharmonicity and Strain Engineering. *ACS Appl. Energy Mater.* **2019**, *2*, 2965−2971.
(54) Tian, B.-Z.; Jiang, X.-P.; Chen, J.; Gao, H.; Wang, Z.-G.; Tang, J.; Zhou, D.-L.; Yang, L.; Chen, Z.-G. Low lattice thermal conductivity and enhanced thermoelectric performance of SnTe via chemical electroless plating of Ag. *Rare Met.* **2022**, *41*, 86−95.
(55) Wang, L.; Hong, M.; Sun, Q.; Wang, Y.; Yue, L.; Zheng, S.; Zou, J.; Chen, Z.-G. Hierarchical Structuring to Break the Amorphous Limit of Lattice Thermal Conductivity in High-Performance SnTe-Based Thermoelectrics. *ACS Appl. Mater. Interfaces* **2020**, *12*, 36370−36379.
(56) Li, Z.; Chen, Y.; Li, J.-F.; Chen, H.; Wang, L.; Zheng, S.; Lu, G. Systhesizing SnTe nanocrystals leading to thermoelectric performance enhancement via an ultra-fast microwave hydrothermal method. *Nano Energy* **2016**, *28*, 78−86.
(57) Han, G.; Zhang, R.; Popuri, S. R.; Greer, H. F.; Reece, M. J.; Bos, J.-W. G.; Zhou, W.; Knox, A. R.; Gregory, D. H. Large-Scale Surfactant-Free Synthesis of p-Type SnTe Nanoparticles for Thermoelectric Applications. *Materials* **2017**, *10*, 233.
(58) Ortega, S.; Ibáñez, M.; Liu, Y.; Zhang, Y.; Kovalenko, M. V.; Cadavid, D.; Cabot, A. Bottom-up engineering of thermoelectric nanomaterials and devices from solution-processed nanoparticle building blocks. *Chem. Soc. Rev.* **2017**, *46*, 3510−3528.
(59) Wang, X.; Han, X.; Du, R.; Xing, C.; Qi, X.; Liang, Z.; Guardia, P.; Arbiol, J.; Cabot, A.; Li, J. Cobalt Molybdenum Nitride-Based Nanosheets for Seawater Splitting. *ACS Appl. Mater. Interfaces* **2022**, *14*, 41924−41933.
(60) Li, M.; Yang, D.; Biendicho, J. J.; Han, X.; Zhang, C.; Liu, K.; Diao, J.; Li, J.; Wang, J.; Heggen, M.; Dunin-Borkowski, R. E.; Wang, J.; Henkelman, G.; Morante, J. R.; Arbiol, J.; Chou, S.-L.; Cabot, A. Enhanced Polysulfide Conversion with Highly Conductive and Electrocatalytic Iodine-Doped Bismuth Selenide Nanosheets in Lithium−Sulfur Batteries. *Adv. Funct. Mater.* **2022**, *32*, 2200529.
(61) Berestok, T.; Chacón-Borrero, J.; Li, J.; Guardia, P.; Cabot, A. Crystalline Magnetic Gels and Aerogels Combining Large Surface Areas and Magnetic Moments. *Langmuir* **2023**, *39*, 3692−3698.
(62) Montaña-Mora, G.; Qi, X.; Wang, X.; Chacón-Borrero, J.; Martinez-Alanis, P. R.; Yu, X.; Li, J.; Xue, Q.; Arbiol, J.; Ibáñez, M.; Cabot, A. Phosphorous incorporation into palladium tin nanoparticles for the electrocatalytic formate oxidation reaction. *J. Electroanal. Chem.* **2023**, *936*, 117369.
(63) He, R.; Yang, L.; Zhang, Y.; Wang, X.; Lee, S.; Zhang, T.; Li, L.; Liang, Z.; Chen, J.; Li, J.; Ostovari Moghaddam, A.; Llorca, J.; Ibáñez, M.; Arbiol, J.; Xu, Y.; Cabot, A. A CrMnFeCoNi high entropy alloy boosting oxygen evolution/reduction reactions and zinc-air battery performance. *Energy Storage Mater.* **2023**, *58*, 287−298.
(64) Yang, D.; Liang, Z.; Tang, P.; Zhang, C.; Tang, M.; Li, Q.; Biendicho, J. J.; Li, J.; Heggen, M.; Dunin-Borkowski, R. E.; Xu, M.; Llorca, J.; Arbiol, J.; Morante, J. R.; Chou, S.-L.; Cabot, A. A High Conductivity 1D π−d Conjugated Metal−Organic Framework with Efficient Polysulfide Trapping-Diffusion-Catalysis in Lithium−Sulfur Batteries. *Adv. Mater.* **2022**, *34*, 2108835.
(65) Zhang, C.; Fei, B.; Yang, D.; Zhan, H.; Wang, J.; Diao, J.; Li, J.; Henkelman, G.; Cai, D.; Biendicho, J. J.; Morante, J. R.; Cabot, A. Robust Lithium−Sulfur Batteries Enabled by Highly Conductive WSe_2-Based Superlattices with Tunable Interlayer Space. *Adv. Funct. Mater.* **2022**, *32*, 2201322.
(66) Yang, D.; Li, M.; Zheng, X.; Han, X.; Zhang, C.; Jacas Biendicho, J.; Llorca, J.; Wang, J.; Hao, H.; Li, J.; Henkelman, G.;

Arbiol, J.; Morante, J. R.; Mitlin, D.; Chou, S.; Cabot, A. Phase Engineering of Defective Copper Selenide toward Robust Lithium−Sulfur Batteries. *ACS Nano* **2022**, *16*, 11102−11114.
(67) Wang, X.; Li, J.; Xue, Q.; Han, X.; Xing, C.; Liang, Z.; Guardia, P.; Zuo, Y.; Du, R.; Balcells, L.; Arbiol, J.; Llorca, J.; Qi, X.; Cabot, A. Sulfate-Decorated Amorphous−Crystalline Cobalt-Iron Oxide Nanosheets to Enhance O−O Coupling in the Oxygen Evolution Reaction. *ACS Nano* **2023**, *17*, 825−836.
(68) Du, R.; Xiao, K.; Li, B.; Han, X.; Zhang, C.; Wang, X.; Zuo, Y.; Guardia, P.; Li, J.; Chen, J.; Arbiol, J.; Cabot, A. Controlled oxygen doping in highly dispersed Ni-loaded g-C_3N_4 nanotubes for efficient photocatalytic H_2O_2 production. *Chem. Eng. J.* **2022**, *441*, 135999.
(69) Wang, X.; Han, X.; Du, R.; Liang, Z.; Zuo, Y.; Guardia, P.; Li, J.; Llorca, J.; Arbiol, J.; Zheng, R.; Cabot, A. Unveiling the role of counter-anions in amorphous transition metal-based oxygen evolution electrocatalysts. *Appl. Catal., B* **2023**, *320*, 121988.
(70) Zhang, Y.; Liu, Y.; Lim, K. H.; Xing, C.; Li, M.; Zhang, T.; Tang, P.; Arbiol, J.; Llorca, J.; Ng, K. M.; Ibáñez, M.; Guardia, P.; Prato, M.; Cadavid, D.; Cabot, A. Tin Diselenide Molecular Precursor for Solution-Processable Thermoelectric Materials. *Angew. Chem., Int. Ed.* **2018**, *130*, 17309−17314.
(71) Zhang, Y.; Liu, Y.; Xing, C. C.; Zhang, T.; Li, M. Y.; Pacios, M.; Yu, X. T.; Arbiol, J.; Llorca, J.; Cadavid, D.; Ibanez, M.; Cabot, A. Tin Selenide Molecular Precursor for the Solution Processing of Thermoelectric Materials and Devices. *ACS Appl. Mater. Interfaces* **2020**, *12*, 27104−27111.
(72) Zuo, Y.; Li, J.; Yu, X.; Du, R.; Zhang, T.; Wang, X.; Arbiol, J.; Llorca, J.; Cabot, A. A SnS_2 Molecular Precursor for Conformal Nanostructured Coatings. *Chem. Mater.* **2020**, *32*, 2097−2106.
(73) Ibáñez, M.; Hasler, R.; Genç, A.; Liu, Y.; Kuster, B.; Schuster, M.; Dobrozhan, O.; Cadavid, D.; Arbiol, J.; Cabot, A.; Kovalenko, M. V. Ligand-Mediated Band Engineering in Bottom-Up Assembled SnTe Nanocomposites for Thermoelectric Energy Conversion. *J. Am. Chem. Soc.* **2019**, *141*, 8025−8029.
(74) Chang, C.; Ibáñez, M. Enhanced Thermoelectric Performance by Surface Engineering in SnTe-PbS Nanocomposites. *Materials* **2021**, *14*, 5416.
(75) Webber, D. H.; Buckley, J. J.; Antunez, P. D.; Brutchey, R. L. Facile dissolution of selenium and tellurium in a thiol−amine solvent mixture under ambient conditions. *Chem. Sci.* **2014**, *5*, 2498−2502.
(76) O'Neill, S. W.; Krauss, T. D. Synthetic Mechanisms in the Formation of SnTe Nanocrystals. *J. Am. Chem. Soc.* **2022**, *144*, 6251−6260.
(77) Shapiro, A.; Jang, Y.; Horani, F.; Kauffmann, Y.; Lifshitz, E. Kirkendall Effect: Main Growth Mechanism for a New SnTe/PbTe/SnO_2 Nano-Heterostructure. *Chem. Mater.* **2018**, *30*, 3141−3149.
(78) Mourdikoudis, S.; Liz-Marzán, L. M. Oleylamine in Nanoparticle Synthesis. *Chem. Mater.* **2013**, *25*, 1465−1476.
(79) García-Rodríguez, R.; Hendricks, M. P.; Cossairt, B. M.; Liu, H.; Owen, J. S. Conversion Reactions of Cadmium Chalcogenide Nanocrystal Precursors. *Chem. Mater.* **2013**, *25*, 1233−1249.
(80) Guo, S.; Fidler, A. F.; He, K.; Su, D.; Chen, G.; Lin, Q.; Pietryga, J. M.; Klimov, V. I. Shape-Controlled Narrow-Gap SnTe Nanostructures: From Nanocubes to Nanorods and Nanowires. *J. Am. Chem. Soc.* **2015**, *137*, 15074−15077.
(81) Lu, W.; He, T.; Li, S.; Zuo, X.; Zheng, Y.; Lou, X.; Zhang, J.; Li, D.; Liu, J.; Tang, G. Thermoelectric performance of nanostructured In/Pb codoped SnTe with band convergence and resonant level prepared via a green and facile hydrothermal method. *Nanoscale* **2020**, *12*, 5857−5865.
(82) Moshwan, R.; Shi, X.-L.; Liu, W.-D.; Yang, L.; Wang, Y.; Hong, M.; Auchterlonie, G.; Zou, J.; Chen, Z.-G. High Thermoelectric Performance in Sintered Octahedron-Shaped $Sn(CdIn)_xTe_{1+2x}$ Microcrystals. *ACS Appl. Mater. Interfaces* **2018**, *10*, 38944−38952.
(83) Wang, L.; Chang, S.; Zheng, S.; Fang, T.; Cui, W.; Bai, P.-p.; Yue, L.; Chen, Z.-G. Thermoelectric Performance of Se/Cd Codoped SnTe via Microwave Solvothermal Method. *ACS Appl. Mater. Interfaces* **2017**, *9*, 22612−22619.
(84) Shen, J.; Cha, J. J. Topological crystalline insulator nanostructures. *Nanoscale* **2014**, *6*, 14133−14140.
(85) Li, Z.; Shao, S.; Li, N.; McCall, K.; Wang, J.; Zhang, S. X. Single Crystalline Nanostructures of Topological Crystalline Insulator SnTe with Distinct Facets and Morphologies. *Nano Lett.* **2013**, *13*, 5443−5448.
(86) Tian, B.-Z.; Jiang, X.-P.; Chen, J.; Gao, H.; Wang, Z.-G.; Tang, J.; Zhou, D.-L.; Yang, L.; Chen, Z.-G. Low lattice thermal conductivity and enhanced thermoelectric performance of SnTe via chemical electroless plating of Ag. *Rare Met.* **2021**, *41*, 86−95.
(87) Haynes, W. M.; Lide, D. R.; Bruno, T. J. *Handbook of Chemistry and Physics*, 97th ed.; CRC Press, 2016; p 2670.
(88) Yin, D.; Dun, C.; Zhang, H.; Fu, Z.; Gao, X.; Wang, X.; Singh, D. J.; Carroll, D. L.; Liu, Y.; Swihart, M. T. Binary and Ternary Colloidal Cu-Sn-Te Nanocrystals for Thermoelectric Thin Films. *Small* **2021**, *17*, 2006729.
(89) Wang, Z.; Ding, L.; Liu, L.; Tan, Z.; Pan, H.; Jiang, P.; Wu, W.; Yu, Y. Grain boundary complexions formed by chemical plating of Cu enhance the thermoelectric properties of $Sn0._{94}Mn_{0.09}Te$. *Scr. Mater.* **2023**, *228*, 115315.
(90) Tan, G.; Zhao, L.-D.; Shi, F.; Doak, J. W.; Lo, S.-H.; Sun, H.; Wolverton, C.; Dravid, V. P.; Uher, C.; Kanatzidis, M. G. High Thermoelectric Performance of p-Type SnTe via a Synergistic Band Engineering and Nanostructuring Approach. *J. Am. Chem. Soc.* **2014**, *136*, 7006−7017.
(91) Li, S. H.; Xin, J. W.; Basit, A.; Long, Q.; Li, S. W.; Jiang, Q. H.; Luo, Y. B.; Yang, J. Y. In Situ Reaction Induced Core−Shell Structure to Ultralow κ_{lat} and High Thermoelectric Performance of SnTe. *Adv. Sci.* **2020**, *7*, 1903493.
(92) Brebrick, R. F.; Strauss, A. J. Anomalous Thermoelectric Power as Evidence for Two-Valence Bands in SnTe. *Phys. Rev.* **1963**, *131*, 104−110.
(93) Banik, A.; Shenoy, U. S.; Anand, S.; Waghmare, U. V.; Biswas, K. Mg Alloying in SnTe Facilitates Valence Band Convergence and Optimizes Thermoelectric Properties. *Chem. Mater.* **2015**, *27*, 581−587.
(94) Liu, X.; Zhang, B.; Chen, Y.; Wu, H.; Wang, H.; Yang, M.; Wang, G.; Xu, J.; Zhou, X.; Han, G. Achieving Enhanced Thermoelectric Performance in $(SnTe)_{1-x}(Sb_2Te_3)_x$ and $(SnTe)_{1-y}(Sb_2Se_3)_y$ Synthesized via Solvothermal Reaction and Sintering. *ACS Appl. Mater. Interfaces* **2020**, *12*, 44805−44814.
(95) Al Rahal Al Orabi, R.; Hwang, J.; Lin, C.-C.; Gautier, R.; Fontaine, B.; Kim, W.; Rhyee, J.-S.; Wee, D.; Fornari, M. Ultralow Lattice Thermal Conductivity and Enhanced Thermoelectric Performance in SnTe:Ga Materials. *Chem. Mater.* **2017**, *29*, 612−620.
(96) Shenoy, U. S.; Bhat, D. K. Bi and Zn co-doped SnTe thermoelectrics: interplay of resonance levels and heavy hole band dominance leading to enhanced performance and a record high room temperature ZT. *J. Mater. Chem. C* **2020**, *8*, 2036−2042.
(97) Bhat, D. K.; Shenoy U, S. High Thermoelectric Performance of Co-Doped Tin Telluride Due to Synergistic Effect of Magnesium and Indium. *J. Phys. Chem. C* **2017**, *121*, 7123−7130.
(98) Bhat, D. K.; Shenoy, U. S. Enhanced thermoelectric performance of bulk tin telluride: Synergistic effect of calcium and indium co-doping. *Mater. Today Phys.* **2018**, *4*, 12−18.
(99) Kim, H.-S.; Gibbs, Z. M.; Tang, Y.; Wang, H.; Snyder, G. J. Characterization of Lorenz number with Seebeck coefficient measurement. *APL Mater.* **2015**, *3*, 041506.
(100) Zhang, M.; Yang, D.; Luo, H.; Liang, Q.; Wu, J.; Tang, X. Super-structured defects modulation for synergistically optimizing thermoelectric property in SnTe-based materials. *Mater. Today Phys.* **2022**, *23*, 100645.
(101) Cahill, D. G.; Watson, S. K.; Pohl, R. O. Lower limit to the thermal conductivity of disordered crystals. *Phys. Rev. B: Condens. Matter Mater. Phys.* **1992**, *46*, 6131−6140.
(102) Chen, Z.; Zhang, X.; Lin, S.; Chen, L.; Pei, Y. Rationalizing phonon dispersion for lattice thermal conductivity of solids. *Natl. Sci. Rev.* **2018**, *5*, 888−894.

(103) Kihoi, S. K.; Shenoy, U. S.; Kahiu, J. N.; Kim, H.; Bhat, D. K.; Lee, H. S. Ultralow Lattice Thermal Conductivity and Enhanced Mechanical Properties of Cu and Sb Co-Doped SnTe Thermoelectric Material with a Complex Microstructure Evolution. *ACS Sustainable Chem. Eng.* **2022**, *10*, 1367−1372.
(104) Banik, A.; Vishal, B.; Perumal, S.; Datta, R.; Biswas, K. The origin of low thermal conductivity in $Sn_{1-x}Sb_xTe$: phonon scattering via layered intergrowth nanostructures. *Energy Environ. Sci.* **2016**, *9*, 2011−2019.
(105) Banik, A.; Ghosh, T.; Arora, R.; Dutta, M.; Pandey, J.; Acharya, S.; Soni, A.; Waghmare, U. V.; Biswas, K. Engineering ferroelectric instability to achieve ultralow thermal conductivity and high thermoelectric performance in $Sn_{1-x}Ge_xTe$. *Energy Environ. Sci.* **2019**, *12*, 589−595.
(106) Chang, C.; Liu, Y.; Lee, S. H.; Spadaro, M. C.; Koskela, K. M.; Kleinhanns, T.; Costanzo, T.; Arbiol, J.; Brutchey, R. L.; Ibáñez, M. Surface Functionalization of Surfactant-Free Particles: a Strategy to Tailor the Properties of Nanocomposites for Enhanced Thermoelectric Performance. *Angew. Chem., Int. Ed.* **2022**, *61*, No. e202207002.

https://doi.org/10.1021/acsami.3c00625
ACS Appl. Mater. Interfaces 2023, 15, 23380−23389